ACS NANO

Editors' Choice

www.acsnano.org

Canine Tongue-Inspired Superspreading-Enhanced Cross Scale-Coupled Evaporation for Thermal Management

Wei Zeng, Yunxiao Li, Yuefeng Gan, Xianfeng Luo, Yun Xing, Zhongpeng Zhu,* Ye Tian,* and Lei Jiang

Cite This: *ACS Nano* 2026, 20, 21281−21293

Read Online

ACCESS | Metrics & More | Article Recommendations | Supporting Information

ABSTRACT: **Overheating is a major cause of device failure. Thin-film evaporative cooling leverages the latent heat of liquid phase change, but its performance is often governed by the balance between interfacial liquid supply and interfacial mass-transfer kinetics. The canine tongue maintains a continuously wetted surface through rapid saliva replenishment and evaporation during thermoregulation. Here, previously unreported nanocilia on the tongue surface of the Beagle (*Canis lupus* familiaris) are identified. These nanocilia coat microscale papillae, revealing a naturally evolved micro−nano hierarchical architecture. Inspired by this architecture, a bioinspired cross-scale continuous surface (BioCCS) integrating microgrooves and nanowires is developed. Microgrooves promote stable liquid spreading, while nanoscale confinement modulates interfacial water interactions and weakens interfacial hydrogen bonding, together establishing a cross-scale coupled evaporation mechanism (CCEM) bridging micro−nano−molecular scales. Tested at 80 °C, a temperature relevant to device reliability, BioCCS achieves an evaporation rate of 31.36 kg h^{-1} m^{-2}, enabling a self-sustained passive cooling system with a 150% enhancement in heat dissipation compared with an unmodified surface. These results provide a concept for autonomously sustained phase change cooling under subboiling conditions.**

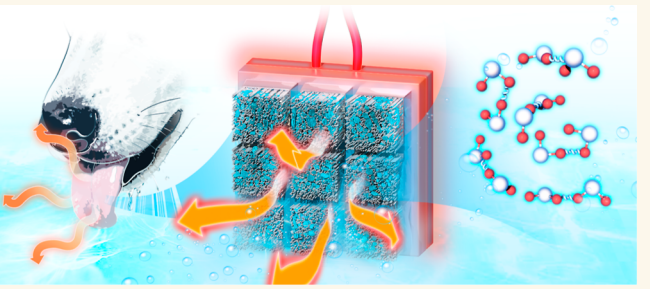

KEYWORDS: *thin-film evaporation, passive cooling, bioinspired surfaces, interfacial water regulation, cross-scale coupled evaporation*

1. INTRODUCTION

Thermal failure has become one of the main causes affecting the performance and reliability of electronic devices as they continue to miniaturize and integrate at higher densities.[1−3] Conventional cooling strategies face intrinsic trade-offs between thermal conductivity, energy consumption, and system integration. For example, air cooling is constrained by its low thermal conductivity and acoustic noise at high flow rates, while liquid cooling requires high pumping power that limits scalability and integration.[4−6] Compared to traditional methods, passive thin-film evaporative cooling leverages the large latent heat of vaporization to achieve a more energy-efficient and environmentally friendly cooling effect under subboiling low-temperature conditions. At the same time, it requires no external energy input, making it an ideal solution for low-power electronic devices.[7−9] However, its performance is constrained by film-scale limits in thickness and stability,[10−15] as well as by an incomplete understanding of molecular evaporation dynamics.[11,16−23] At the mesoscale, thick liquid films introduce high interfacial heat resistance, whereas thin films near contact lines tend to dry out. At the molecular level, evaporation requires water molecules to overcome strong hydrogen-bond interactions within the liquid. These multiscale challenges collectively influence the interfacial evaporation dynamics, and without systematically regulating the gas−liquid−solid interfacial layers, efforts to improve thin-film evaporative cooling efficiency will remain incomplete.

Researchers have widely explored structured surfaces to mitigate these challenges.[24,25] Nanostructured surfaces, such as nanowire arrays, enhance wicking and reduce liquid-film heat resistance.[11,26−28] Hybrid micro−nano textures accelerate spreading and avoid local dryout.[29,30] Patterned capillaries balance evaporation with rewetting to improve stability.[31,32] Collectively, these approaches regulate the interface and improve heat dissipation. Although substantial advances have

Received: April 1, 2026
Revised: June 24, 2026
Accepted: June 25, 2026
Published: July 22, 2026

https://doi.org/10.1021/acsnano.6c06165
ACS Nano 2026, 20, 21281−21293

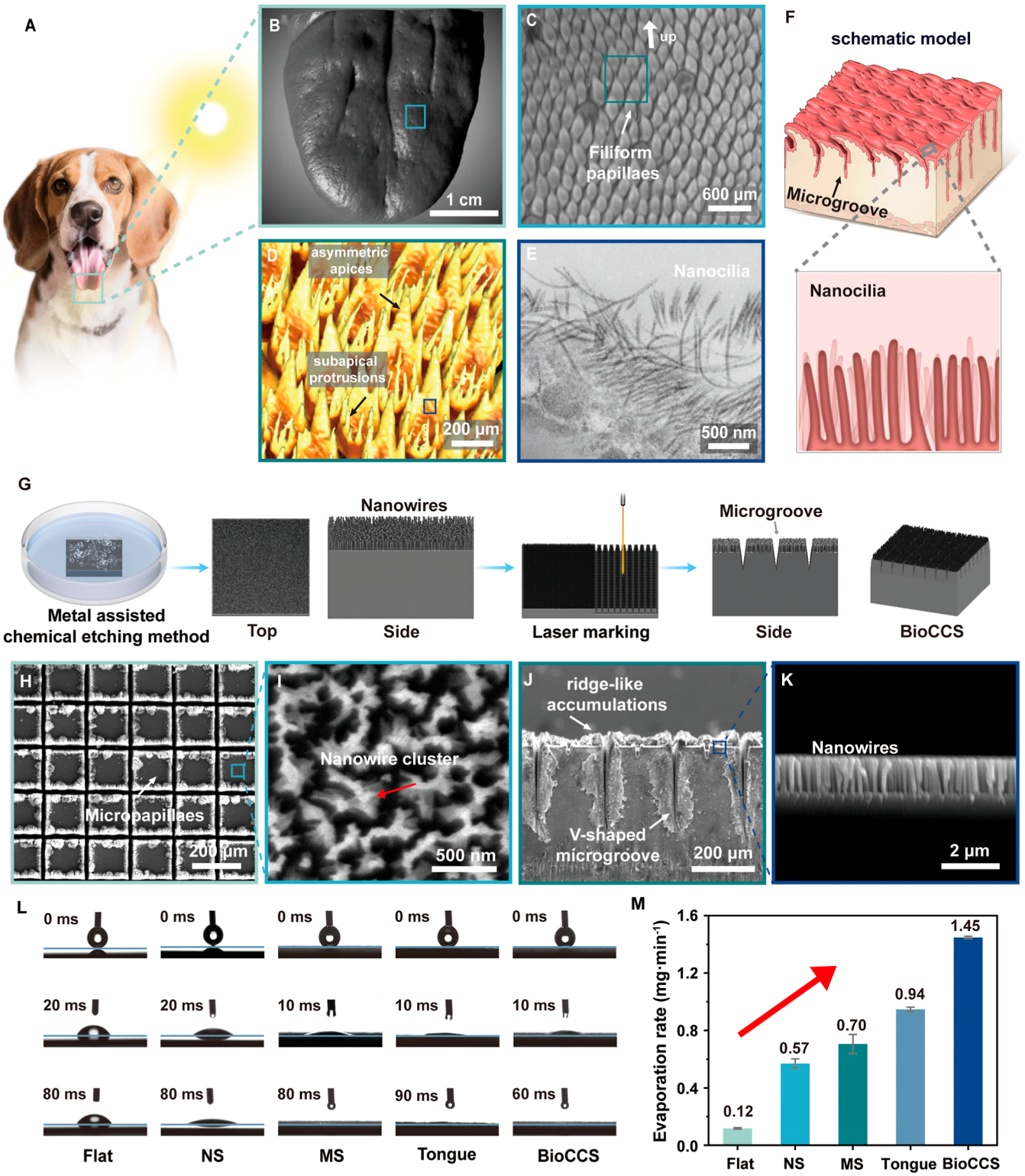

Figure 1. Multiscale structural features of canine tongue and bioinspired design of BioCCS. (A) Schematic of saliva-driven evaporative cooling on the canine tongue. (B–E) Multiscale characterization of natural papillae. Micro-CT reveals regularly arranged filiform papillae (187.8 ± 5.2 μm in diameter, 179.8 ± 1.2 μm in height, 34.8 ± 0.4 μm spacing) with asymmetric apexes and circumferential subapical protrusions. TEM identifies dense nanocilia (790.4 ± 25.3 nm length) covering papillary surfaces. (F) Three-dimensional schematic of the hierarchical tongue architecture. (G–K) Fabrication and morphology of BioCCS. Laser micromachining and chemical etching yield micropapillae (~200 μm height) interconnected by V-shaped microgrooves (~30 μm base width) and uniformly decorated nanowires (~100 nm diameter, 1 μm height, ~30% porosity). SEM images show ordered micropapillary arrays and porous nanowire networks, with partial nanowire aggregation forming clusters. (L) Dynamic wetting behavior characterized by the evolution of the contact angle. FS and NS exhibit slower wetting kinetics, whereas MS, BioCCS and natural tongue achieve superspreading (θ < 5°) within 90 ms. (M) Evaporation rate comparison. BioCCS provides 11.2-fold higher evaporation flux than FS and outperforms both NS and MS controls, demonstrating synergistic micro–nano enhancement.

https://doi.org/10.1021/acsnano.6c06165
ACS Nano 2026, 20, 21281–21293

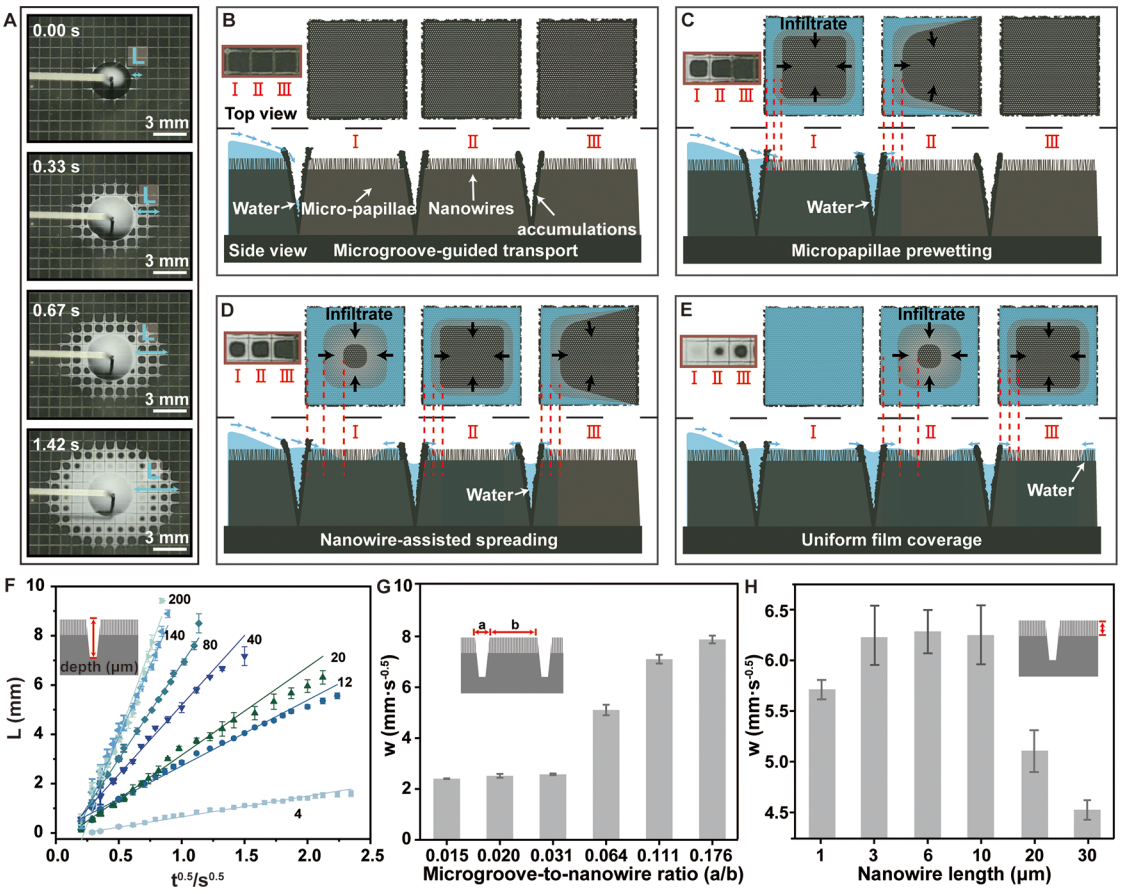

Figure 2. Modulation of liquid spreading dynamics on BioCCS. (A) Time-resolved images of water spreading across BioCCS. (B–E) Sequential spreading stages: (B) Microgroove-guided transport, where capillary action drives rapid liquid advance along grooves; (C) Micropapilla prewetting, with peripheral nanowire Regions prewet first, leading to slower penetration; (D) Nanowire-assisted spreading, as capillary-driven films advance across papillae; (E) Uniform film coverage, with uniform films extending to adjacent papillae. (F) Penetration length (L) increases with groove depth, yielding a maximum wicking coefficient of 11.09 mm $s^{-0.5}$ at 200 μm. (G) Increasing the micro–nano structural ratio enhances capillary wicking. (H) Nanowire height optimizes spreading, with performance maximized at 10 μm and decreasing for taller wires.

been made in optimizing interfacial performance, the mechanistic understanding of how structural hierarchy couples with molecular interactions remains incomplete. Despite extensive efforts, establishing a unified framework that connects micro–nano structures with molecular-level evaporation dynamics continues to pose a major challenge. Natural systems, however, have long evolved to coordinate transport and phase-change processes across scales, offering inspiration for linking structural hierarchy with molecular-level regulation.

Canines, which have sweat glands mainly in their paw pads and nose, dissipate heat primarily through saliva evaporation from their tongue. Here we identify previously undescribed nanocilia decorating hierarchical filiform papillae on the canine tongue. Although microgrooves and nanostructures have been extensively explored in engineered systems, such approaches typically emphasize geometric optimization and performance metrics. In contrast, the canine tongue shows an evolutionarily stable hierarchy, where microscale papillae are seamlessly integrated with nanoscale features. The long-term persistence of this architecture in vivo indicates its potential relevance to interfacial processes. Guided by this natural template, we developed a bioinspired cross-scale continuous surface (BioCCS) integrating microgrooves with nanowire arrays. Through spreading and transport measurements, structural analysis, and spectroscopic probing of hydrogen-bond states, we uncovered a Cross-Scale Coupled Evaporation Mechanism (CCEM). In this mechanism, capillary transport cooperates with nanoscale molecular regulation to facilitate evaporation. Furthermore, we designed a bioinspired passive cooling system in which the evaporator maintains a stable heat dissipation capacity through self-sustained liquid from contact with a lower reservoir. Under the same condition of no additional power consumption, this system overcomes the instability of coolant supply in traditional passive evaporative cooling systems. At the failure threshold of 80 °C, it achieves a heat dissipation capacity of 5 W cm^{-2}, significantly outperforming unmodified surfaces with a 150% increase in heat dissipation. The BioCCS evaporator shows potential as an efficient and environmentally friendly solution for passive sub-boiling thermal management.

2. RESULTS AND DISCUSSION

2.1. Bioinspired Design from Canine Tongue Structures

Beagles (*Canis lupus* familiaris) cool mainly through saliva evaporation from the tongue (Figure 1A), indicating an ultraefficient heat dissipation capacity.[33,34] In this study, the morphology of canine tongue was systematically examined using micro–computed tomography (micro-CT), scanning

https://doi.org/10.1021/acsnano.6c06165
ACS Nano 2026, 20, 21281–21293

electron microscopy (SEM) (Figure S1), and transmission electron microscopy (TEM). These analyses revealed the previously uncharacterized cross-scale structural characteristics that nanocilia decorate filiform papillae and form a hierarchy that promotes liquid transport and evaporation which results in the ultraefficient heat dissipation capacity.[35−38] Micro-CT showed filiform papillae with an average diameter of 187.7 ± 5.2 μm and a height of 179.8 ± 1.2 μm, separated by grooves of 34.8 ± 0.4 μm (Figures 1B,C, S2). Papillae showed asymmetric apexes with circumferential conical protrusions (Figure 1D). At the nanoscale, SEM and TEM identified dense nanocilia (28.1 ± 1.0 nm in diameter and 790.4 ± 25.3 nm in length) covering papillary surfaces (Figures 1E, S3). These findings demonstrate hierarchical coupling of micro- and nanoscale structures that support liquid transport and evaporation.

Inspired by these hierarchical features, we extracted a three-dimensional biological model consisting of microscale grooves and nanowire arrays (Figure 1F). To translate this biological model into an engineered surface, we adopted a two-step fabrication process (Figure 1G). First, metal-assisted chemical etching generated well-aligned silicon nanowire arrays with a controlled etching rate of 0.55 μm min^{-1} (Figure S4). Next, high-precision laser micromachining created microgrooves with tunable geometries. The depth increased by approximately 3 μm with each laser pass, allowing precise structural control (Figure S5). The resulting BioCCS exhibited a unit size of 154 μm, with conical protrusions surrounding each pillar and V-shaped microgrooves (30 μm top width) between them. Pillar surfaces were uniformly decorated with clustered nanowire arrays (1 μm height, 29% porosity). The spacing between neighboring nanowire clusters was on the order of several hundred nanometers, whereas the nanowires within each cluster were densely packed, resulting in substantially reduced local spacing. Laser processing also induced nanoparticle deposition along micropapillae edges, forming ridge-like accumulations (Figure 1H−K).

The functional consequences of this design were assessed by liquid spreading and evaporation tests. Thin-film evaporative cooling depends on both wetting dynamics and phase-change rate.[39,40] Compared with flat surface (FS) and nanostructured surface (NS), BioCCS and microstructured surface (MS) showed rapid superhydrophilic wetting, confirming the dominant role of microscale grooves in liquid uptake (Figure 1L). Evaporation experiments showed that BioCCS achieved an evaporation rate of 1.45 mg min^{-1}, which was 11.2-fold higher than planar surfaces and 54% greater than the natural tongue (Figure 1M). The pronounced enhancement reflects engineered capillarity and demonstrates that artificial multiscale architectures can surpass biological benchmarks. Evaporation rate serves as a direct indicator of phase-change efficiency, expressed by the vapor mass flux. Although both surfaces exhibited comparable macroscopic spreading, BioCCS maintained more stable liquid films and faster evaporation, indicating that nanoscale structures provide additional regulation beyond geometric effects. This enhancement reflects a strong coupling between capillary-driven liquid transport and interfacial evaporation.

3. SPREADING DYNAMICS ON BIOCCS

To investigate the role of hierarchical structures in liquid spreading, we analyzed the dynamic wetting behavior of water droplets on FS, NS, MS, and BioCCS. Even with reduced microgroove depth and density, BioCCS maintained uniform thin liquid films (Figure 2A). In contrast, FS exhibited limited liquid spreading capability due to the absence of an effective capillary network. NS promoted liquid-film spreading only through localized capillary effects, while its long-range liquid transport capability remained limited. The interconnected microgrooves on MS generated strong capillary forces that enabled rapid long-distance liquid transport, with discrete droplet deposition still observable on distal micropapillae. However, the transported liquid remained primarily confined within the microgrooves, making it difficult to establish a continuous and uniform thin liquid film across the entire surface. By integrating microscale capillary transport with nanoscale liquid-film regulation, BioCCS achieved synergistic control of continuous liquid replenishment and uniform thin-film coverage, thereby exhibiting interfacial superspreading behavior (Figure S6).

Systematic variation of surface parameters delineated four spreading regimes controlled by hierarchical micro−nano structures, comprising microgroove-guided transport, micropapilla prewetting, nanowire-assisted spreading, and uniform film coverage, that collectively facilitated interfacial superspreading. Upon contact (Figure 2B), capillary forces rapidly moved liquid through the groove network around adjacent micropapillae. During this stage, the liquid traveled 1.45 mm in 41 ms. As the liquid spread outward, it was simultaneously drawn upward by the ridge-like accumulations along the microgroove edges (Figure 2C). The liquid penetrated the nanowire arrays on micropapilla I, producing optical contrast in which bright regions corresponded to thin liquid films, whereas dark regions denoted unwetted nanowires. After 167 ms, the liquid advanced another 1 mm, indicating slower transport within the nanowire scaffold (Figure 2D). As spreading continued, liquid moved 1 mm within 333 ms, forming complete coverage on micropapilla I and then propagating across micropapillae II and III in a repeating sequence (Figure 2E). Such a transition reveals the synergistic regulation between microgrooves and nanowires in directing liquid transport.

To further interpret the spreading dynamics, we employed the Lucas−Washburn capillary model, which describes liquid penetration in porous structures.[41,42] According to this model, the penetration length L increases proportionally with the square root of time ($L \propto t^{1/2}$). On this basis, the capillary suction coefficient w is defined as

$$w = \frac{L}{t^{1/2}} \tag{1}$$

where L denotes the penetration length of the liquid front and t represents time. The parameter w has units of mm s$^{-1/2}$ and characterizes effective capillary suction, reflecting structure and viscous dissipation. An increase in w corresponds to stronger capillary-driven spreading, resulting in faster and more efficient liquid transport. This formulation enables quantitative comparison across structures. Figure 2F shows how the penetration length L evolves over time for different groove depths. With a constant nanowire height of 10 μm and a fixed micro−nano ratio of 0.064, w increased significantly as the microgroove depth increased from 4 to 200 μm. At an optimal depth of 140 μm, w reached 10.90 mm s$^{-1/2}$, a 15.4-fold increase compared with the baseline value of 0.72 mm s$^{-1/2}$ at 4 μm. Further increasing the depth to 200 μm provided only a marginal gain (~9.7%), reaching 11.09 mm s$^{-1/2}$. The

https://doi.org/10.1021/acsnano.6c06165
ACS Nano 2026, 20, 21281−21293

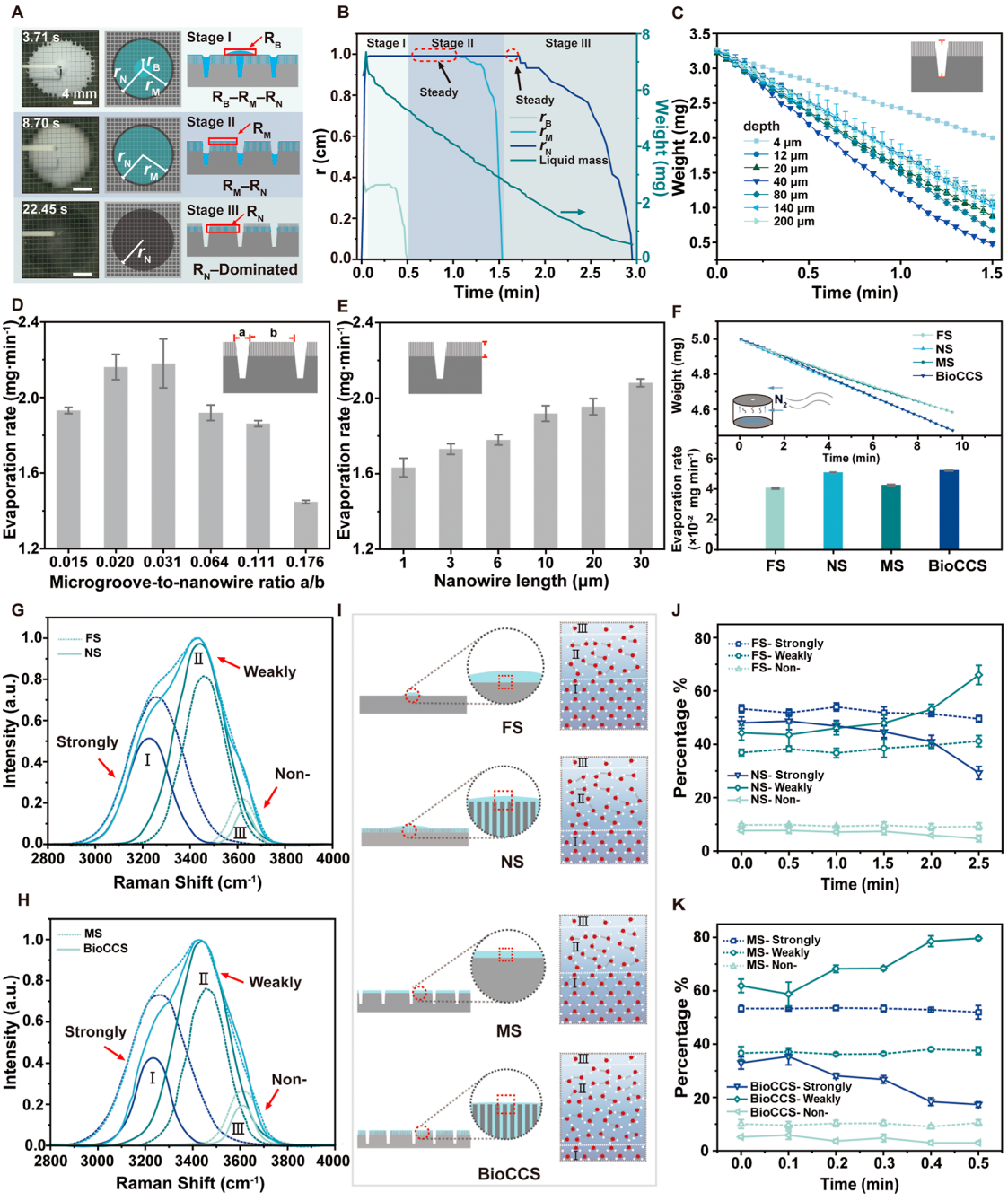

Figure 3. Cross-Scale Coupled Evaporation Mechanism on BioCCS. (A) Evaporation proceeds through three stages: Stage I, coexistence of macroscopic bulk-liquid evaporation region (Region R_B), microgroove-regulated evaporation region (Region R_M), and nanowire-dominated evaporation region (Region R_N); Stage II, coexistence of Regions R_M and R_N; and Stage III, an RN-dominated evaporation stage. (B) Temporal evolution of characteristic radii and total liquid mass during evaporation. The shaded regions denote the three evaporation stages (Stage I–III) identified from the dynamic evolution of the characteristic radii. Steady-state analysis indicates that R_N yields the highest area-normalized flux (1.98 mg min^{-1} cm^{-2}). (C–E) Structural regulation of evaporation (C) Evaporation rate peaks at a groove depth of 40 μm (1.92 mg min^{-1}) and declines for deeper grooves. (D) The micro–nano ratio increases the rate from 1.93 to 2.18 mg min^{-1} as it rises from 0.015 to 0.031, beyond which performance is suppressed. (E) Increasing nanowire height (1–30 μm) monotonically raises the rate from 1.63 to 2.08 mg min^{-1}. (F) TGA mass-loss curves and the corresponding evaporation rates indicate that the presence of nanowire structures alters the interfacial evaporation dynamics. (G–I) Raman O–H spectra show that the O–H stretching band is deconvoluted into three components: (I) ~3200 cm^{-1} (strongly hydrogen-bonded water), (II) 3400–3500 cm^{-1} (weakly hydrogen-bonded water), and (III) 3600–3650 cm^{-1} (non-hydrogen-bonded water). The fraction of strongly hydrogen-bonded water decreases markedly on nanostructured surfaces, from 49.6% on FS and 52.0% on MS to 29.3% on NS, while BioCCS exhibits the lowest proportion (17.4%). This reduction relative to NS is consistent with microgroove-assisted liquid transport, which concentrates evaporation within the nanowire-confined Region. (J–K) BioCCS maintains the lowest fraction of strongly hydrogen-bonded water throughout the evaporation process.

optimized micro–nano architecture showed a 72.9-fold higher wicking coefficient than NS (Figure S6).

With groove depth fixed at 40 μm (Figure 2G), increasing the micro–nano ratio from 0.015 to 0.17 elevated w from 2.40

https://doi.org/10.1021/acsnano.6c06165
ACS Nano 2026, 20, 21281–21293

to 7.10 mm $s^{-1/2}$, indicating groove-dominated capillary spreading and improved film coverage. Finally, Figure 2H illustrates the synergistic and antagonistic roles of nanostructures. For nanowires shorter than 10 μm, capillary forces acted synergistically with microgrooves, maintaining w between 5.71 and 6.28 mm $s^{-1/2}$. In this regime, the short nanowires enhanced liquid guidance and strengthened capillary-driven spreading. However, when nanowire height exceeded 10 μm, excessive viscous dissipation suppressed lateral flow, reducing w to 4.52 mm $s^{-1/2}$ and thereby inhibiting capillary spreading efficiency.[43] Together, these observations and analyses establish practical design principles for hierarchical surfaces. Moderate groove depths enhance in-plane liquid spreading, whereas precise control of nanowire dimensions maximizes capillary-driven spreading without added viscous losses.

4. EVAPORATION MECHANISMS ON BIOCCS

To further elucidate how spreading contributes to enhanced evaporation, we first examined the temporal evolution of the spreading radius during droplet expansion. Three coupled evaporation modes governed by microgroove−nanowire interactions are identified. Initially, three characteristic radii coexist, corresponding to an R_B−R_M−R_N coexistence stage. The three radii are defined as follows: the bulk-liquid radius (r_B), representing the macroscopic bulk-liquid evaporation region (Region R_B); the microgroove-replicated thin-film radius (r_M), corresponding to the microgroove-regulated evaporation region (Region R_M); and the nanowire-confined thin-film radius (r_N), denoting the nanowire-dominated evaporation region (Region R_N). As evaporation proceeds, liquid transfer from R_B to $_{RM}$ and R_N establishes a quasi-steady state characterized by R_M−R_N coexistence, which ultimately converges to an R_N-dominated stage in which R_N serves as the sole evaporating zone (Figure 3A). This multistage evolution aligns with classical thin-film evaporation theory, which divides the liquid film near a solid interface into three regions according to thickness and dominant transport resistance. The bulk-liquid region, characterized by a thick film and high thermal resistance, contributes little to overall evaporation. The transition-film region of intermediate thickness serves as the main evaporation pathway, whereas the adsorbed ultrathin film at the molecular scale contributes minimally due to strong solid−liquid interactions. In our experiments, Region R_B corresponds to the bulk-liquid zone, Region R_M maps to the transition film driven by microgroove-induced expansion, and Region R_N represents a confined transition film penetrating the nanowire scaffold. Unlike conventional planar transition films, R_N initially forms as a micrometer-thick liquid layer continuous with R_M but spatially restricted by the nanoscale framework. Such confinement modifies both transport resistance and interfacial molecular interactions, establishing R_N as a nanowire-confined transition-film regime responsible for the dominant evaporation contribution under steady conditions.

High-precision measurements further reveal distinct dynamics between Regions R_M and R_N. Once the characteristic radii r_B, r_M, and r_N stabilize or approach zero, the system enters steady stages. At the steady stages (Figure 3B), the total evaporation rate ($\dot{m}$) can be expressed as

$$\dot{m} = J_B \cdot A_B + J_M \cdot A_M + J_N \cdot A_N \cdot P_N + J_G \cdot A_G \quad (2)$$

where A_B, A_M, A_N, and A_G are the wetted surface areas of Regions R_B, R_M, R_N, and microgroove interior, respectively, all defined along the projected plane parallel to the substrate; J_B, J_M, J_N, and J_G are the corresponding evaporation fluxes (mg min^{-1} cm^{-2}) evaluated over the same projected areas; and P_N is the nanowire porosity (P_N = 0.29). In Stage II, the evaporation rate can be approximated as $\dot{m}_1 \approx J_M \cdot A_M + J_N \cdot A_N \cdot P_N$, and in Stage III, only the R_N film remains, giving $\dot{m}_2 \approx J_N \cdot A_N \cdot P_N$. The contribution of liquid residing inside the microgrooves is neglected in the simplified expressions for Stages II and III because it is substantially smaller than the contributions from Regions R_M and R_N. This simplification is justified for two reasons. First, during evaporation, the small amount of liquid initially stored in the grooves is rapidly imbibed into Region R_N or redistributed as a thin film on Region R_M. Second, previous studies have shown that the evaporation flux from the groove interior is negligible compared with those from A_M and A_N.[44−47]

Region R_M contributes a higher absolute evaporation rate, whereas Region R_N achieves greater efficiency, with a normalized flux of 1.98 mg min^{-1} cm^{-2} (Figure S7), approximately three times that of Region R_M. This enhancement can be partially rationalized by the Kelvin equation: the high interfacial curvature in R_N increases the local saturation vapor pressure, thereby promoting molecular escape.[48−51] However, order-of-magnitude estimates based on the Kelvin equation suggest that explaining the approximately 3-fold evaporation flux of R_N relative to R_M solely through the Kelvin effect would require confinement approaching sub-10 nm length scales (Supporting Information, Figure S8). Such a discrepancy indicates that factors beyond the classical Kelvin effect may contribute to the enhanced evaporation behavior in R_N, including nanoconfinement-induced modulation of interfacial water. To further account for the observed enhancement, the influence of microgroove−nanowire geometry and the resulting redistribution of liquid films is examined in the following parametric analysis.

Enhanced efficiency primarily arises from hierarchical micro−nano geometry that optimizes transport and stabilizes film evaporation. Increasing microgroove depth from 4 to 40 μm raises the evaporation rate from 0.80 to 1.91 mg min^{-1}, but deeper grooves (>40 μm) trap liquid, increasing film thickness and reducing the evaporation efficiency (Figure 3C). These results reveal a supply−resistance competition, where deeper grooves increase capillary replenishment but concurrently thicken the liquid film and lengthen the vapor escape path, raising interfacial transport resistance. Beyond microgroove effects, a similar trade-off emerges in the micro−nano ratio. Raising the ratio from 0.015 to 0.031 boosts the evaporation rate from 1.93 to 2.18 mg min^{-1}, whereas a further increase to 0.17 causes an approximately 33% decline due to excess groove storage and an insufficient nanowire areal fraction that limits effective evaporation sites (Figure 3D). The enhancement−suppression trend is inconsistent with a monotonic curvature argument, since a higher nanowire fraction should increase interfacial curvature and, consequently, enhance evaporation through the kelvin effect. Nanowire height further illustrates this effect, as increasing the height from 1 to 30 μm steadily raises the evaporation rate from 1.63 to 2.08 mg min^{-1}, reflecting enhanced vertical transport and improved film uniformity (Figure 3E). Taken together, these geometric effects enable BioCCS to achieve a 17.2-fold increase in evaporation rate relative to FS (0.12 mg min^{-1}) under ambient conditions.

https://doi.org/10.1021/acsnano.6c06165
ACS Nano 2026, 20, 21281−21293

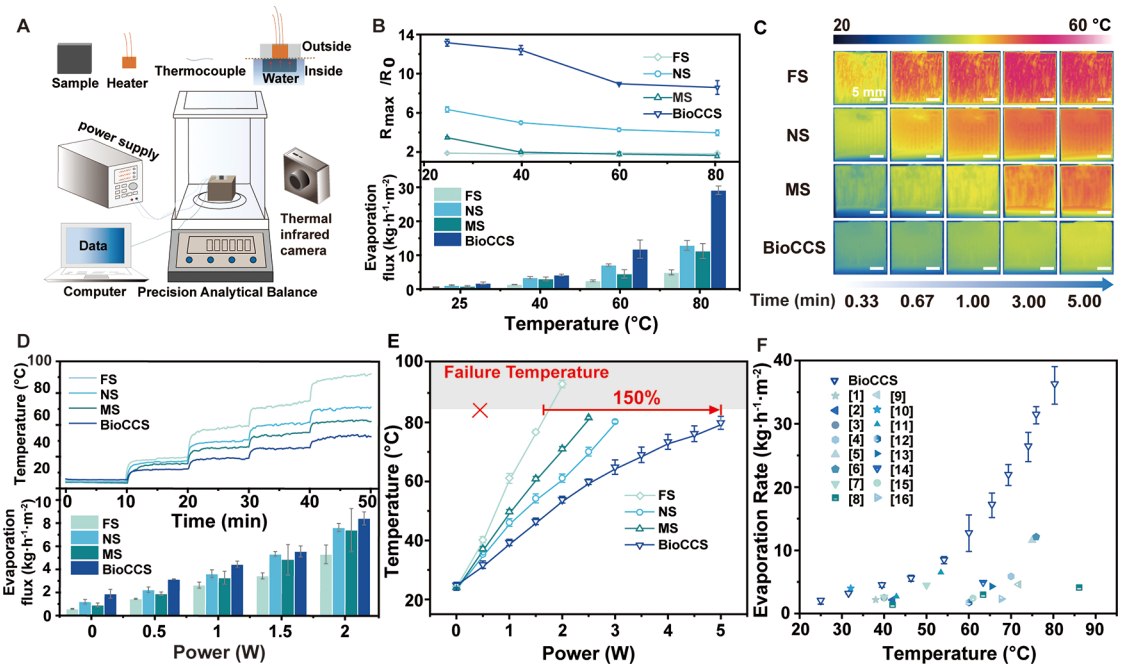

Figure 4. Heat−mass transfer and thermal dissipation of the BioCCS Evaporator. (A) Schematic of the experimental system for evaporation and passive heat-transfer characterization. (B) Temperature-dependent evaporation performance (25−80 °C). BioCCS shows the most stable spreading and evaporation among FS, NS and MS. (C) Infrared thermography at 1.5 W shows an about 10 °C lower surface temperature than FS, while BioCCS maintains spatial uniformity within the Region of interest (variation <1.5 °C). (D) Under 0−2 W heat input, BioCCS consistently attains the lowest steady-state temperature. (E) At an industrially safe operating temperature below 85 °C, BioCCS dissipates an input power of 5 W, achieving 150% higher effective heat removal than FS. (F) Benchmarking against reported interfacial evaporators indicates that the BioCCS delivers thermal performance across 25−80 °C.

To further investigate the interfacial evaporation dynamics, we employed thermogravimetric analysis (TGA) to analyze the variation of droplet mass over time. This method minimizes the influence of macroscopic factors, such as spreading area, vapor retention, and film morphology, on the results. The findings indicate that, compared to FS and MS, the evaporation rate of NS and BioCCS with nanostructures (Figure 3F) increased by 20%. This difference may be due to the disturbance of nanostructures in the thin liquid film evaporation zone near the three-phase contact line, which alters the interfacial evaporation dynamics. The observed variation suggests that nanoscale confinement influences the local state of interfacial water, thereby affecting the evaporation dynamics near the three-phase contact line.

In situ Raman spectroscopy conducted at the final stage of evaporation, where the influence of bulk water is minimized, reveals distinct changes in molecular bonding states within the confined liquid. The spectrum collected immediately before the disappearance of the liquid-related Raman signal was used to characterize the interfacial water state. Nanostructures markedly decrease the fraction of strongly hydrogen-bonded water (O−H peak ~3200 cm^{-1}) to 29.3% on NS versus 49.6% on FS, and 17.4% on BioCCS versus 52.0% on MS (Figure 3G,H). The O−H stretching frequency inversely correlates with bond strength,[52,53] with lower-frequency bands corresponding to more strongly bonded water molecules. Therefore, the observed reduction in the low-frequency component indicates a substantial decrease in strongly hydrogen-bonded water and a corresponding shift toward less strongly bonded water states. As strongly hydrogen-bonded water largely determines the stability of the interfacial hydrogen-bond network, the observed redistribution weakens the overall intermolecular interactions within the interfacial water layer, thereby facilitating the escape of water molecules from the evaporation interface and promoting evaporation. This interpretation is consistent with the changes in evaporation dynamics observed by TGA. These findings establish a direct connection between molecular-scale water-state regulation and interfacial evaporation dynamics.

Beyond this overall trend, comparative Raman analysis further elucidates how micro−nano coupling amplifies this effect during evaporation. Compared with FS, NS already exhibits a substantial decrease in strongly bonded water (49.6% to 29.3%), confirming that nanoscale confinement intrinsically weakens the hydrogen-bond network.[16,54−57] In contrast, MS shows negligible change relative to FS, indicating that microstructures alone do not significantly alter molecular bonding states. When microgrooves are integrated with nanowires in BioCCS, the fraction of strongly bonded water further decreases to 17.4%, about 40% lower than on NS (Figure 3I). This amplification arises from rapid capillary replenishment of liquid from Region R_B to the R_M and R_N zones, which prevents the buildup of thick overlying layers and maintains a thin, dynamically renewed film at the nanowire interface (Figure S9). Such continuous replenishment reinforces nanoscale confinement throughout the evaporation process, enabling BioCCS to sustain the lowest fraction of strongly bonded water across all stages (Figure 3J,K).

Based on the above analysis, we propose the CCEM, in which hierarchical synergy operates simultaneously at the micro-, nano-, and molecular levels. At the microscale, interconnected grooves and ridge-like protrusions along papillary edges enable efficient capillary pumping, rapidly transporting liquid from Region R_B toward the active

https://doi.org/10.1021/acsnano.6c06165
ACS Nano 2026, 20, 21281−21293

evaporation zones (R_M and R_N). At the nanoscale, confined nanowire arrays modulate the interfacial hydrogen-bond network and reorganize the interfacial liquid into a dynamic, weakly bonded layer. The capillary delivery from microgrooves reinforces this nanoscale regulation by relieving bulk-liquid constraints, maintaining an energetically favorable interfacial state for evaporation. At the molecular level, the disrupted hydrogen-bond network alters the interfacial evaporation dynamics, thereby enabling higher evaporation flux per unit area. The CCEM elucidates the multiscale origin of evaporation on BioCCS, and provides a generalizable design principle for engineering next-generation evaporation interfaces with tunable efficiency.

5. PERFORMANCE OF BIOCCS EVAPORATORS

Through systematic variation of micro−nano parameters, an optimized interface with 40 μm-deep grooves (micro−nano ratio = 0.064) and 10 μm-high nanowires was obtained. These optimized structural parameters were selected based on a combined evaluation of capillary-driven liquid transport and evaporation performance. Lower micro−nano ratios weakened liquid replenishment, whereas excessive groove fractions promoted liquid retention and reduced evaporation efficiency. Therefore, a micro−nano ratio of 0.064 provided the best balance between continuous liquid supply and efficient evaporation. Characterization showed a wicking coefficient of 5.10 mm $s^{-1/2}$ and a single-droplet evaporation rate of 1.92 mg min^{-1}, thereby reflecting synergistic enhancement of liquid spreading and evaporation. To quantitatively characterize passive evaporation, we constructed a dedicated experimental system (Figure 4A) designed to simulate spontaneous liquid transport and evaluate the thermal performance of the bioinspired cooling surface. The test sample was vertically fixed in a water reservoir, with its lower end immersed in water to enable spontaneous liquid uptake and its upper end exposed with a fixed area for evaporation. A thin, equal-area heating film was attached to the back and powered by an adjustable DC supply. Temperature was monitored in real time using a thermocouple fixed at the center of the film−sample interface. The system allowed precise control over the test area, immersion depth, and input power. The setup was positioned on a precision balance for real-time mass monitoring, and all leads were rigidly secured to minimize vibration-induced errors. This design utilizes inherent spreading−evaporation coupling, enabling passive mass/heat characterization without external pumping.

Temperature-dependent tests showed the most stable spreading and evaporation on BioCCS, in contrast to FS, MS and NS. Even when the droplet showed poor contact on FS, BioCCS maintained uniform liquid spreading across the interface, indicating strong antidewetting stability (Figure S10). At 80 °C, the BioCCS evaporator exhibited an evaporation rate 5.9, 1.6, and 1.3 times higher than those of FS, MS, and NS, respectively (Figure 4B). Thermal-stability tests yielded a mass flux of 31.36 kg h^{-1} m^{-2} at 80 °C, confirming substantial enhancement over controls.

Infrared thermography under 1.5 W heating was performed on FS and MS, which were coated with emissivity-matched layers to ensure accurate temperature comparison. The results revealed distinct thermal characteristics (Figure 4C). BioCCS was ∼10 °C cooler than FS, exceeding the reductions observed for NS (∼3 °C) and MS (∼4 °C). The surface temperature variation across BioCCS remained below 1.5 °C, demonstrating stable thermal distribution. The microgroove structures of MS enable capillary flow but lack nanoscale features for evaporation enhancement. In contrast, NS provides evaporation capacity but suffers from inadequate liquid replenishment due to weak capillary action. The performance enhancement of BioCCS originates from its hierarchical microgroove−nanowire architecture. The 40 μm-deep grooves provide efficient vertical transport, counteracting gravity and viscous losses to maintain continuous wetting. Simultaneously, the 10 μm nanowire array promotes thin-film evaporation, increasing evaporative flux.

Systematic characterization across 0−2 W input power revealed BioCCS consistently exhibited lower steady-state temperatures. The heat removed by evaporation increases linearly with the evaporation flux. Under identical input power, similar evaporation fluxes were observed across all surfaces, suggesting that most of the applied heat is dissipated through phase change (Figure 4D, Materials and Methods). However, BioCCS maintained this thermodynamic dissipation at the lowest surface temperature, demonstrating superior heat-transfer efficiency. At the widely accepted safety threshold of 85 °C for industrial chips,[58] the BioCCS evaporator sustained a heat input of 5 W through passive phase-change cooling, representing a 150% improvement over FS (2 W) and markedly exceeding NS (3 W) and MS (2.5 W) evaporators (Figures 4E, S11). Under industry-relevant limits (40−85 °C),[58] the BioCCS evaporator exhibited an extended thermal margin. As shown in Figure 4F, compared with recently reported interface-enhanced evaporators (Table S1), BioCCS evaporator achieved higher evaporation across the tested temperatures, particularly at 60−80 °C.[59−74] This enhancement stems from synergy between microgroove-driven liquid replenishment and nanowire-facilitated film spreading, which suppressed high-temperature dewetting and maintained a uniform evaporating interface. In summary, the BioCCS evaporator mitigates the instability of working fluids in conventional passive evaporative cooling by autonomously regulating the replenishment-evaporation process. It offers great potential for application in the field of passive heat dissipation in integrated devices under sub-boiling conditions.

6. CONCLUSIONS

Based on systematic microscopic analyses, this study revealed previously unreported dense nanofibrillar structures on the filiform papillae of the canine tongue, which inspired the design of BioCCS. By analyzing the evolution of liquid films, mass variation, and molecular reorganization during spreading and evaporation on BioCCS across scales from the macroscopic to the molecular level, we proposed the CCEM. This mechanism elucidates the synergistic coupling among capillary liquid replenishment, thin-film expansion, and molecular hydrogen-bond reorganization, deepening the understanding of multiscale interfacial phase-change and heat-transfer coupling. Guided by the CCEM, the optimized BioCCS evaporator exhibits enhanced liquid spreading, evaporation, and passive cooling performance. Compared to the single NS structure, the capillary wicking coefficient of BioCCS was 72.9 times higher. In the critical temperature range of 60−80 °C, the evaporation rate was 1−2 times higher than that of recently reported interfacial evaporation−enhanced surfaces. During passive operation without external energy input, the system sustained a heat load of 5 W without failure (below 85 °C), corresponding to a 150% increase compared with the

https://doi.org/10.1021/acsnano.6c06165
ACS Nano 2026, 20, 21281−21293

unmodified surface. Nevertheless, the organization and dynamics of interfacial molecules are influenced not only by geometric structures but also by surface chemical composition and energy distribution. The current CCEM primarily focuses on the physical coupling between the structure and interfacial water molecules, while the chemical aspects of interfacial molecular behavior remain less explored. Future studies should aim to tune water−substrate interactions through interfacial chemical modification at the molecular level to further enhance evaporation efficiency and energy utilization. Overall, this work bridges the gap in understanding cross-scale coupling by establishing a unified framework that integrates liquid spreading dynamics with intermolecular structural rearrangement. It demonstrates that hierarchical structures, with micron-scale grooves facilitating liquid replenishment and nanostructures modulating interfacial water states, synergistically enhance evaporation efficiency. This provides a theoretical basis for designing and optimizing self-sustained passive evaporation heat dissipation interfaces, with potential applications in bioinspired thermal management, desalination, and energy-conversion technologies.

7. METHODS

7.1. Materials

Hydrofluoric acid (40%, HF), isoamyl acetate, osmium tetroxide (1%), and lead citrate were purchased from Aladdin (Shanghai, China). Ethanol (absolute), acetone, silver nitrate ($AgNO_3$, analytical grade) and nitric acid (65−68%, HNO_3) were obtained from Sinopharm (Shanghai, China). Glutaraldehyde solution (2.5%) and phosphate-buffered saline (PBS, pH 7.0) were purchased from Solarbio (Beijing, China), and 10% neutral buffered formalin was from Sigma-Aldrich (USA). Uranyl acetate was obtained from Ruen (USA) and epoxy embedding resin (Epon 812) was used as received. Deionized water (>18 MΩ cm) was used throughout.

7.2. Animal Tissue Collection

Canine tongue tissues were obtained from Beijing Huchi Biotechnology Co., Ltd. (Beijing, China). All live-animal procedures were performed solely by the supplier at its licensed facility, in accordance with institutional IACUC guidelines and national Regulations on the Administration of Laboratory Animals, and under the approval of the Animal Welfare and Ethics Committee of Beijing Fangyuan Yuan Breeding Farm (approval FYY-LLS-20230705). Male beagles (∼10 kg; n = 1; 10−12 months) were used; tissues were excised post-mortem and fixed in 10% neutral buffered formalin prior to transfer. The authors conducted no live-animal work and handled only fixed, deidentified specimens.

7.3. SEM Sample Preparation

Tongue tissues were rinsed with PBS and fixed in 2.5% glutaraldehyde (Solarbio, Beijing) for 2 h at room temperature, then stored at 4 °C. After graded ethanol dehydration and isoamyl acetate (Aladdin, Shanghai) transition, samples were critical-point dried (Autosamdri-931, Tousimis), mounted on aluminum stubs, sputter-coated with gold (∼8 nm, 20 mA, 60 s; VTA MSP-1S), and imaged under high-vacuum mode on a Quattro S environmental SEM (10 kV, working distance 8 mm).

7.4. MicroCT Characterization

Nondestructive three-dimensional imaging of the canine tongue papillae was performed using a ZEISS Xradia 615 Versa micro−computed tomography system. High- and low-resolution scans (voxel size: 3−45 μm) were conducted under optimized voltage and power settings. The reconstructed tomographic image stacks were imported into Dragonfly software (Object Research Systems, Canada) for three-dimensional segmentation and visualization. Using volume rendering and Region-based segmentation, the barbed (filiform) papillae were extracted to visualize their three-dimensional spatial arrangement and interpapillary connectivity.

7.5. TEM Sample Preparation

Canine tongue tissues were received in 2.5% glutaraldehyde fixative at 4 °C. Fixed tissues were removed from the primary fixative and rinsed three times in 0.1 M phosphate buffer (pH 7.0) for 15 min each. The samples were then postfixed in 1% osmium tetroxide for 1−2 h, followed by three additional buffer rinses (15 min each). Subsequently, the specimens were dehydrated through a graded ethanol series (30%, 50%, 70%, 80%, 90%, and 95%; 15 min each), followed by two changes of 100% ethanol (20 min each) and two changes of acetone. Resin infiltration proceeded in acetone: epoxy resin mixtures at 1:1 (v/v) for 1 h and 3:1 (v/v) for 2 h, then 100% resin overnight. Infiltrated tissues were embedded and polymerized at 70 °C overnight to obtain resin blocks. Ultrathin sections (70−90 nm) were cut on a Leica EM UC7 ultramicrotome and collected on copper grids. Sections were double-stained with uranyl acetate (2%) and lead citrate, with intermediate washes in 50% ethanol and distilled water (5−10 min each) before imaging. Grids were examined on a Hitachi HT7800 transmission electron microscope (accelerating voltage 120 kV, bright-field).

7.6. Fabrication of BioCCS and Control Surfaces

Silicon wafers (2 × 2 cm^2) were ultrasonically cleaned in acetone, ethanol, and deionized water (10 min each). Native oxide was removed with 40% HF (1 min, fume hood), followed by Ag-assisted chemical etching to form silicon nanowires (SiNWs): 0.02 M $AgNO_3$ and 4.8 M HF for 18 min at 23 °C, yielding ∼10 μm SiNWs (consistent with ∼0.557 μm min^{-1}). Residual Ag was removed in HNO_3 (65−68%) diluted 1:1, 5 min, then thoroughly rinsed. Microgrooves were patterned on SiNWs using a fiber laser marking system (WM-N3000A, HSET). The laser micromachining parameters were as follows: marking speed of 200 mm s^{-1}, repetition rate of 60 kHz, and laser power set to 32% of the rated output. Other timing parameters were kept constant according to the instrument's standard configuration. The groove depth increased by ∼3 μm per laser pass as measured by SEM cross sections. After rinsing and drying, hybrid surfaces were denoted BioCCS; the control surfaces were FS (bare silicon), MS (microgrooves only), and NS (SiNWs only).

7.7. Wettability Measurements

Droplets (2 μL) were deposited on surfaces, and spreading dynamics were recorded using a contact angle goniometer (LSA100, LAUDA Scientific, Germany) at 100 fps. Dynamic spreading characterization was carried out by recording the spreading process of 4 μL droplets using a Nikon D7000 with a Laowa macro lens under LED illumination at 24 fps. Unless otherwise specified, measurements were performed under ambient laboratory conditions (23 ± 1 °C, 25 ± 5% RH).

7.8. Single-Droplet Evaporation Rate

Droplets (4 μL) were dispensed by an injection pump (TJ-4A, LongerPump) at 0.5 μL s^{-1} using a 33G needle onto test surfaces placed on a precision balance (MS105DU, Mettler Toledo; 0.01 mg resolution) within a draft shield. To stabilize the ambient humidity, self-indicating silica gel (S821279, Sinopharm Chemical Reagent Co., Ltd.) was placed inside the balance chamber, without affecting the weighing process. The evaporation rate was calculated as the slope of the linear portion of the mass-loss curve with respect to time, expressed in units of mg min^{-1}. Mass data were recorded at 1 Hz intervals.

7.9. Thermogravimetric Analysis

Structured silicon substrates of different configurations (FS, NS, MS, and BioCCS) were laser-cut to 3.5 × 3.5 mm^2 to fit the TGA crucibles, ensuring full coverage of the structured area by the deposited droplet and minimizing the influence of surface wettability differences among samples. Water droplets (5−6 μL) were analyzed on a TG 209 F3 Tarsus (NETZSCH) at 35 °C under isothermal conditions. The instrument was operated with nitrogen protective gas (balance line) and purge gas (sample line), each at 20 mL min^{-1}; the

https://doi.org/10.1021/acsnano.6c06165
ACS Nano 2026, 20, 21281−21293

lines were purged for at least 10 min before each run. Open Al_2O_3 pans were used unless otherwise noted, owing to their chemical inertness and thermal stability. TGA was used to obtain mass-loss kinetics.[75]

7.10. Raman Spectroscopy

Raman spectra were collected using a Renishaw in situ Raman microscope with a 532 nm excitation laser and a 50 times objective (laser power ~0.5 mW at the sample). A 5 μL water droplet was placed on each surface, and O−H stretching bands (2800−4000 cm^{-1}) were monitored continuously during evaporation. The O−H stretching band (2800−4000 cm^{-1}) was deconvolved using pseudo-Voigt functions in Origin (OriginLab) to quantitatively analyze different hydrogen-bonding states of interfacial water, including peaks centered at approximately 3200 cm^{-1}, 3400 cm^{-1}, and 3600 cm^{-1}, which correspond to strongly hydrogen-bonded water, weakly hydrogen-bonded water, and non−hydrogen-bonded water, respectively.

7.11. Infrared Thermography

Samples (2 × 2 cm^2) were bonded to 2 × 2 cm^2 polyimide heating films and driven by a DC power supply (eTM-305MP, eTOMMENS). With an immersion depth of 1 mm, surface temperatures were recorded using an infrared camera (MAG-F6, MAGNITY). To minimize emissivity differences, FS and MS were blackened with an oil-based black marker on dry, nonwetted Regions; NS and BioCCS were left uncoated. Coatings were allowed to dry completely and did not contact liquid. The camera emissivity parameter was set to 0.95 for all measurements, and infrared camera readings were calibrated against a T-type thermocouple placed at the center of the heated area. Temperatures were extracted from a 2 × 1.8 cm^2 temperature measurement area corresponding to the heater footprint, with camera−sample distance and viewing angle kept constant. The stripe-like features observed in MS infrared images originate from anisotropic reflection along the microgrooves. Because the oil-based black coating could partially suppress capillary wicking, it was used only for emissivity unification in qualitative visualization. Accurate temperature values were obtained from T-type thermocouples, while infrared thermography was employed solely for qualitative and approximate quantitative analysis.

7.12. Passive Heat- and Mass-Transfer Tests

Samples (2 × 2 cm^2) were bonded to 1 × 1 cm^2 polyimide heating films on the backside and fixed within custom 3D-printed holders (P1S, Bambu Lab) through internal support structures. The holders securely positioned each sample in a vertical orientation, with the structured front surface facing outward and fully exposed to air, the backside (with the heater attached) not in contact with water. Vertically inserted into a water reservoir to an immersion depth of 1 cm, the assembly exposed a 1 × 1 cm^2 evaporation area corresponding to the heater footprint on the backside. A precision balance was used for real-time mass monitoring, while a DC power supply (eTM-305MP, eTOMMENS) delivered electrical input to the heater. Surface temperature was measured at the center using a T-type thermocouple (SUP-R200T, Supmea) attached to the heated area. Input power was increased stepwise from 0 to 5 W in 0.5 W increments. Each step was held 10 min or until steady state, defined as $|\Delta T| < 1$ °C over 3 min and a near-linear mass-loss trace. Mass-loss data from the balance were synchronized with the thermocouple-based temperature measurements. Ambient humidity inside the balance chamber was stabilized using the same silica-gel approach as described for single-droplet evaporation measurements. Where reported, the heat flux (q'') was determined as $q'' = \frac{mL}{tA}$ where m is the evaporated mass, t is the evaporation time, A is the exposed area, and L is the latent heat of vaporization of water. Thus, q'' is directly proportional to the evaporation flux (m/tA).

7.13. Statistical Analysis

All data are presented as mean ± SD from at least three independent samples unless otherwise stated. Statistical analyses were descriptive, focusing on comparative trends across temperature and surface types. Linear fitting was applied where appropriate, and R^2 values were reported without inferential testing.

■ ASSOCIATED CONTENT

Supporting Information

The Supporting Information is available free of charge at https://pubs.acs.org/doi/10.1021/acsnano.6c06165.

Supporting Text on curvature and kelvin effect analysis, SEM, TEM, and micro-CT characterization of the canine tongue surface, fabrication and structural characterization of BioCCS and control surfaces, liquid spreading dynamics, evaporation performance and stage analysis, multiscale nanowire spacing characterization, thermal management performance evaluation (Figures S1−S11), and summary of reported evaporation rates on structured surfaces (Table S1) (PDF) (PDF)

■ AUTHOR INFORMATION

Corresponding Authors

Zhongpeng Zhu − *State Key Laboratory of Bioinspired Interfacial Materials Science, School of Chemistry and Materials Science, University of Science and Technology of China, Hefei, Anhui 230026, China;* orcid.org/0009-0005-5464-4375; Email: zhuzp@ustc.edu.cn

Ye Tian − *Key Laboratory of Bio-inspired Materials and Interfacial Science, Technical Institute of Physics and Chemistry, Chinese Academy of Sciences, Beijing 100190, P. R. China*; Email: tianye@mail.ipc.ac.cn

Authors

Wei Zeng − *State Key Laboratory of Bioinspired Interfacial Materials Science, School of Chemistry and Materials Science, University of Science and Technology of China, Hefei, Anhui 230026, China*

Yunxiao Li − *State Key Laboratory of Bioinspired Interfacial Materials Science, School of Chemistry and Materials Science, University of Science and Technology of China, Hefei, Anhui 230026, China*

Yuefeng Gan − *State Key Laboratory of Bioinspired Interfacial Materials Science, School of Nano Science and Technology, Suzhou Institute for Advanced Research, University of Science and Technology of China, Suzhou, Jiangsu 215123, China*

Xianfeng Luo − *Key Laboratory of Bio-inspired Materials and Interfacial Science, Technical Institute of Physics and Chemistry, Chinese Academy of Sciences, Beijing 100190, P. R. China*

Yun Xing − *State Key Laboratory of Bioinspired Interfacial Materials Science, School of Chemistry and Materials Science, University of Science and Technology of China, Hefei, Anhui 230026, China*

Lei Jiang − *State Key Laboratory of Bioinspired Interfacial Materials Science, School of Chemistry and Materials Science, University of Science and Technology of China, Hefei, Anhui 230026, China; State Key Laboratory of Bioinspired Interfacial Materials Science, School of Nano Science and Technology, Suzhou Institute for Advanced Research, University of Science and Technology of China, Suzhou, Jiangsu 215123, China; Key Laboratory of Bio-inspired Materials and Interfacial Science, Technical Institute of Physics and Chemistry, Chinese Academy of Sciences, Beijing 100190, P. R. China*

https://doi.org/10.1021/acsnano.6c06165
ACS Nano 2026, 20, 21281−21293

Complete contact information is available at:
https://pubs.acs.org/10.1021/acsnano.6c06165

Author Contributions

Conceptualization: Z.Z., W.Z., and L.J. Methodology: W.Z., and Z.Z. Investigation: W.Z., Z.Z., Y.L., Y.G., Y.X., X.L., and Y.T. Visualization: W.Z., and Z.Z. Supervision: Z.Z. Writing (original draft): W.Z. Writing (review and editing): Z. Z., W. Z., and Y. L. Micro-CT imaging in this article was performed by Wenjie Cao and Wen Shi (Carl Zeiss (Shanghai) Co. Ltd.).

Funding

This work was supported by the Science Fund for Creative Research Groups of the National Natural Science Foundation of China (No. 22521103), the Innovative and Entrepreneurial Talent Plan of Jiangsu (JSSCRC2023554), the Leading Talents of Innovation and Entrepreneurship of Gusu District (ZXL2023182), and the Suzhou Key Laboratory of Bioinspired Interface Science Fund (SZ2024004).

Notes

The authors declare no competing financial interest.

■ ACKNOWLEDGMENTS

The authors acknowledge the technical support from Carl Zeiss (Shanghai) Co., Ltd. For micro-CT imaging and the experimental support from the Physical and Chemical Analysis Center, Suzhou Institute for Advanced Research, University of Science and Technology of China.

■ REFERENCES

(1) Dhumal, A. R.; Kulkarni, A. P.; Ambhore, N. H. A Comprehensive Review on Thermal Management of Electronic Devices. *J. Eng. Appl. Sci.* **2023**, *70*, 140.
(2) Song, I. T.; Kang, J.; Koh, J.; Choi, H.; Yang, H.; Park, E.; Lee, J.; Cho, W.; Lee, Y. M.; Lee, S.; Kim, N.; Lee, M.; Kim, K. Thermal Runaway Prevention Through Scalable Fabrication of Safety Reinforced Layer in Practical Li-Ion Batteries. *Nat. Commun.* **2024**, *15*, 8294.
(3) Xian, J. W.; Xu, Y. L.; Stoyanov, S.; Coyle, R. J.; Dunne, F. P. E.; Gourlay, C. M. The Role of Microstructure in the Thermal Fatigue of Solder Joints. *Nat. Commun.* **2024**, *15*, 4258.
(4) Zhang, Z.; Wang, X.; Yan, Y. A Review of the State-of-the-Art in Electronic Cooling. *e-Prime - Adv. Electr. Eng. Electron. Energy* **2021**, *1*, 100009.
(5) Chakraborty, S.; Shukla, D.; Panigrahi, P. K. A Review on Coolant Selection for Thermal Management of Electronics and Implementation of Multiple-Criteria Decision-Making Approach. *Appl. Therm. Eng.* **2024**, *245*, 122807.
(6) Li, J.; Fu, Y.; Zhou, J.; Yao, K.; Ma, X.; Gao, S.; Wang, Z.; Dai, J.; Lei, D.; Yu, X. Ultrathin, Soft, Radiative Cooling Interfaces for Advanced Thermal Management in Skin Electronics. *Sci. Adv.* **2023**, *9*, No. eadg1837.
(7) Li, J.; Wang, X.; Liang, D.; Xu, N.; Zhu, B.; Li, W.; Yao, P.; Jiang, Y.; Min, X.; Huang, Z.; Zhu, S.; Fan, S.; Zhu, J. A Tandem Radiative/Evaporative Cooler for Weather-Insensitive and High-Performance Daytime Passive Cooling. *Sci. Adv.* **2022**, *8*, No. eabq0411.
(8) Fei, J.; Zhang, X.; Han, D.; Lei, Y.; Xie, F.; Zhou, K.; Koh, S. W.; Ge, J.; Zhou, H.; Wang, X.; et al. Passive Cooling Paint Enabled by Rational Design of Thermal-Optical and Mass Transfer Properties. *Science* **2025**, *388*, 1044−1049.
(9) Huang, K.; Lan, H.; Li, S.; Tan, R.; Si, Y.; Lei, L.; Wang, K.; Xu, X.; Fang, W.; Liang, X.; Li, W. J.; Hu, J. Advanced Evaporative Cooling Materials: From Designs to Applications. *Prog. Mater. Sci.* **2025**, *154*, 101504.
(10) Jiang, M.; Wang, Y.; Liu, F.; Du, H.; Li, Y.; Zhang, H.; To, S.; Wang, S.; Pan, C.; Yu, J.; Quéré, D.; Wang, Z. Inhibiting the Leidenfrost Effect Above 1,000 Degrees C for Sustained Thermal Cooling. *Nature* **2022**, *601*, 568−572.
(11) Feng, T.; Pei, Y.; Zhang, H.; Asai, B.; Dong, G.; Joshi, A.; Saha, A.; Cai, S.; Chen, R. High-Flux and Stable Thin-Film Evaporation from Fiber Membranes with Interconnected Pores. *Joule* **2025**, *9*, 101975.
(12) Liu, H. R.; Wang, C. X.; Li, B. J.; Hua, L.; Yu, J. Q.; Wang, R. Z. Reversible Sweat Cooling on Mobile Electronic Devices by Metal-Organic Frameworks-Based Moisture Sorption-Desorption Process. *Mater. Today Nano* **2022**, *18*, 100198.
(13) Liu, X.; Yang, J.; Zou, Q.; Hu, Y.; Li, P.; Tan, L.; Miljkovic, N.; Yang, R. Enhancing Liquid-Vapor Phase-Change Heat Transfer with Micro/nano-Structured Surfaces. *ACS Nano* **2025**, *19*, 9513−9589.
(14) Aryana, K.; Gaskins, J. T.; Nag, J.; Stewart, D. A.; Bai, Z.; Mukhopadhyay, S.; Read, J. C.; Olson, D. H.; Hoglund, E. R.; Howe, J. M.; Giri, A.; Grobis, M. K.; Hopkins, P. E. Interface Controlled Thermal Resistances of Ultra-Thin Chalcogenide-Based Phase Change Memory Devices. *Nat. Commun.* **2021**, *12*, 774.
(15) Zhakhovsky, V. V.; Kryukov, A. P.; Levashov, V. Y.; Shishkova, I. N.; Anisimov, S. I. Mass and Heat Transfer Between Evaporation and Condensation Surfaces: Atomistic Simulation and Solution of Boltzmann Kinetic Equation. *Proc. Natl. Acad. Sci. U.S.A.* **2019**, *116*, 18209−18217.
(16) Xia, Q.; Pan, Y.; Liu, B.; Zhang, X.; Li, E.; Shen, T.; Li, S.; Xu, N.; Ding, J.; Wang, C.; et al. Solar-Driven Abnormal Evaporation of Nanoconfined Water. *Sci. Adv.* **2024**, *10*, No. eadj3760.
(17) Fang, S.; Li, J.; Xu, Y.; Shen, C.; Guo, W. Evaporating Potential. *Joule* **2022**, *6*, 690−701.
(18) Nagata, Y.; Usui, K.; Bonn, M. Molecular Mechanism of Water Evaporation. *Phys. Rev. Lett.* **2015**, *115*, 236102.
(19) Loche, P.; Bonthuis, D. J.; Netz, R. R. Molecular Dynamics Simulations of the Evaporation of Hydrated Ions from Aqueous Solution. *Commun. Chem.* **2022**, *5*, 55.
(20) Tan, J. Y.; Brata, J. J.; Fei, J.; Ge, J.; Song, M.; Zhang, X.; Zou, G.; Koh, S. W.; Gao, H.; Li, S.; Li, H. Electrostatic Field-Enabled Ultra-Efficient Evaporative Cooling. *Nat. Commun.* **2025**, *16*, 8046.
(21) Rana, B.; Fairhurst, D. J.; Jena, K. C. Investigation of Water Evaporation Process at Air/Water Interface Using Hofmeister Ions. *J. Am. Chem. Soc.* **2022**, *144*, 17832−17840.
(22) He, X.; Wang, Z.; Geng, Z.; Liu, J.; Jin, Z.; Chen, N. Superoxide Radicals Inducing Perturbation in Water Hydrogen Bond Networks for Enhanced Solar-driven Water Evaporation. *Adv. Funct. Mater.* **2025**, *35*, 2505818.
(23) Huang, X.; Zhu, J.; Wu, D.; Zhang, Q.; Nie, Z. Surface-engineered Solar-driven Interfacial Evaporation: Innovations and Challenges. *Adv. Mater. Interfaces* **2025**, *12*, 2300371.
(24) Wen, R.; Ma, X.; Lee, Y.-C.; Yang, R. Liquid-Vapor Phase-Change Heat Transfer on Functionalized Nanowired Surfaces and Beyond. *Joule* **2018**, *2*, 2307−2347.
(25) Inanlu, M. J.; Ganesan, V.; Upot, N. V.; Wang, C.; Suo, Z.; Fazle Rabbi, K.; Kabirzadeh, P.; Bakhshi, A.; Fu, W.; Thukral, T. S.; et al. Unveiling the Fundamentals of Flow Boiling Heat Transfer on Micronanostructured Surfaces. *Sci. Adv.* **2024**, *10*, No. eadp8632.
(26) Lee, J.; Suh, Y.; Dubey, P. P.; Barako, M. T.; Won, Y. Capillary Wicking in Hierarchically Textured Copper Nanowire Arrays. *ACS Appl. Mater. Interfaces* **2019**, *11*, 1546−1554.
(27) Chun, J.; Xu, C.; Zhang, Y.; Li, Q.; Wen, R.; Ma, X. Fast Capillary Wicking on Hierarchical Copper Nanowired Surfaces with Interconnected V-Grooves: Implications for Thermal Management. *ACS Appl. Nano Mater.* **2021**, *4*, 5360−5371.
(28) Hsu, W.-T.; Shim, D. I.; Yun, M.; Lee, D.; Kim, B. S.; Cho, H. H. Free-Standing Nanowire Printed Surfaces with High Variability in Substrate Selection for Boiling Heat Transfer Enhancement. *Int. J. Heat Mass Transfer* **2023**, *212*, 124313.
(29) Xu, Z.; Zhang, P.; Yu, C.; Miao, W.; Chang, Q.; Qiu, M.; Li, Y.; Tian, Y.; Jiang, L. Liquid-Superspreading-Boosted High-Performance Jet-Flow Boiling for Enhancement of Phase-Change Cooling. *Adv. Mater.* **2023**, *35*, No. e2210557.

(30) Song, Y.; Diaz-Marin, C. D.; Zhang, L.; Cha, H.; Zhao, Y.; Wang, E. N. Three-Tier Hierarchical Structures for Extreme Pool Boiling Heat Transfer Performance. *Adv. Mater.* **2022**, *34*, No. e2200899.
(31) Li, W.; Yang, S.; Chen, Y.; Li, C.; Wang, Z. Tesla Valves and Capillary Structures-Activated Thermal Regulator. *Nat. Commun.* **2023**, *14*, 3996.
(32) Li, W.; Li, C.; Wang, Z.; Chen, Y. Enhanced Flow Boiling in Microchannels Integrated with Supercapillary Pinfin Fences. *Int. J. Heat Mass Transfer* **2022**, *183*, 122185.
(33) Goldberg, M. B.; Langman, V. A.; Taylor, C. R. Panting in Dogs: Paths of Air Flow in Response to Heat and Exercise. *Respir. Physiol.* **1981**, *43*, 327−338.
(34) Blatt, C. M.; Taylor, C. R.; Habal, M. B. Thermal Panting in Dogs: The Lateral Nasal Gland, a Source of Water for Evaporative Cooling. *Science* **1972**, *177*, 804−805.
(35) Haggag, T.; Mahmoud, E. F.; Salem, Z. A.; AbuBakr, N. Comparative Evaluation of the Ultrastructural Morphology and Distribution of Filiform and Fungiform Tongue Papillae in Egyptian Mice, Fruit Bats and Long-Eared Hedgehogs. *Anat. Cell Biol.* **2020**, *53*, 493−501.
(36) Emura, S.; Tamada, A.; Hayakawa, D.; Chen, H.; Shoumura, S. Morphology of the Dorsal Lingual Papillae in the Bush Dog (Speothos Venaticus). *Okajimas Folia Anat. Jpn.* **2000**, *77*, 137−141.
(37) Singh, B. B.; Boshell, J. L.; Steflik, D. E.; McKinney, R. V., Jr. A Correlative Light Microscopic, Scanning and Transmission Electron Microscopic Study of the Dog Tongue Filiform Papillae. *Scan. Electron Microsc.* **1980**, *3*, 511−515.
(38) Zhang, C.; Wu, Z.; Che, Z.; Li, X.; Sun, Y.; Ren, L. Liquid Spreading on a Pre-Wetted Biomimetic Surface Inspired by a Dog's Tongue. *Sci. China: Technol. Sci.* **2016**, *59*, 738−748.
(39) Craster, R. V.; Matar, O. K. Dynamics and Stability of Thin Liquid Films. *Rev. Mod. Phys.* **2009**, *81*, 1131−1198.
(40) Li, J.; Kang, D.; Rabbi, K. F.; Fu, W.; Yan, X.; Fang, X.; Fan, L.; Miljkovic, N. Liquid Film−induced Critical Heat Flux Enhancement on Structured Surfaces. *Sci. Adv.* **2021**, *7*, No. eabg4537.
(41) Abadi, G. B.; Bahrami, M. The Effect of Surface Roughness on Capillary Rise in Micro-Grooves. *Sci. Rep.* **2022**, *12*, 14867.
(42) Cai, J.; Jin, T.; Kou, J.; Zou, S.; Xiao, J.; Meng, Q. Lucas-Washburn Equation-Based Modeling of Capillary-Driven Flow in Porous Systems. *Langmuir* **2021**, *37*, 1623−1636.
(43) Wei, H.; Dandey, V. P.; Zhang, Z.; Raczkowski, A.; Rice, W. J.; Carragher, B.; Potter, C. S. Optimizing "Self-Wicking" Nanowire Grids. *J. Struct. Biol.* **2018**, *202*, 170−174.
(44) Wang, H.; Garimella, S. V.; Murthy, J. Y. Characteristics of an Evaporating Thin Film in a Microchannel. *Int. J. Heat Mass Transfer* **2007**, *50*, 3933−3942.
(45) Zhou, W.; Hu, X.; He, Y.; Yu, Y.; Mao, L. Study on Axial Wetting Length and Evaporating Heat Transfer in Rectangular Microgrooves with Superhydrophilic Nano-Textured Surfaces for Two-Phase Heat Transfer Devices. *Energy Convers. Manage.* **2019**, *200*, 112098.
(46) Ranjan, R.; Murthy, J. Y.; Garimella, S. V. Analysis of the Wicking and Thin-Film Evaporation Characteristics of Microstructures. *J. Heat Transfer* **2009**, *131*, 101001.
(47) Plawsky, J. L.; Fedorov, A. G.; Garimella, S. V.; Ma, H. B.; Maroo, S. C.; Chen, L.; Nam, Y. Nano- and Microstructures for Thin-Film Evaporation—a Review. *Nanoscale Microscale Thermophys. Eng.* **2014**, *18*, 251−269.
(48) Fisher, L. R.; Gamble, R. A.; Middlehurst, J. The Kelvin Equation and the Capillary Condensation of Water. *Nature* **1981**, *290*, 575−576.
(49) Malijevsky, A.; Parry, A. O. Modified Kelvin Equations for Capillary Condensation in Narrow and Wide Grooves. *Phys. Rev. Lett.* **2018**, *120*, 135701.
(50) Mitropoulos, A. The Kelvin Equation. *J. Colloid Interface Sci.* **2008**, *317*, 643−648.
(51) Yang, Q.; Sun, P. Z.; Fumagalli, L.; Stebunov, Y. V.; Haigh, S. J.; Zhou, Z. W.; Grigorieva, I. V.; Wang, F. C.; Geim, A. K. Capillary Condensation Under Atomic-Scale Confinement. *Nature* **2020**, *588*, 250−253.
(52) Walrafen, G. E. Raman Spectral Studies of Water Structure. *J. Chem. Phys.* **1964**, *40*, 3249−3256.
(53) Wang, Y. H.; Zheng, S.; Yang, W. M.; Zhou, R. Y.; He, Q. F.; Radjenovic, P.; Dong, J. C.; Li, S.; Zheng, J.; Yang, Z. L.; Attard, G.; Pan, F.; Tian, Z. Q.; Li, J. F. In Situ Raman Spectroscopy Reveals the Structure and Dissociation of Interfacial Water. *Nature* **2021**, *600*, 81−85.
(54) Zhang, Q.; Gao, B.; Zhang, L.; Liu, X.; Cui, J.; Cao, Y.; Zeng, H.; Xu, Q.; Cui, X.; Jiang, L. Anomalous Water Molecular Gating from Atomic-Scale Graphene Capillaries for Precise and Ultrafast Molecular Sieving. *Nat. Commun.* **2023**, *14*, 6615.
(55) Gao, Y.; Chen, Z.; Zhang, Y.; Wen, Y.; Yu, X.; Shan, B.; Xu, B.; Chen, R. Reorientation of Hydrogen Bonds Renders Unusual Enhancement in Thermal Transport of Water in Nanoconfined Environments. *Nano Lett.* **2024**, *24*, 5379−5386.
(56) Bie, C.; Yang, J.; Zeng, X.; Wang, Z.; Sun, X.; Yang, Z.; Yu, J.; Zhang, X. Nanoconfinement Effects in Electrocatalysis and Photocatalysis. *Small* **2025**, *21*, No. e2411184.
(57) Byl, O.; Liu, J.; Wang, Y.; Yim, W.; Johnson, J. K.; Yates, J. T. Unusual Hydrogen Bonding in Water-Filled Carbon Nanotubes. *J. Am. Chem. Soc.* **2006**, *128*, 12090−12097.
(58) McCluskey, P.; Mensah, K.; O'Connor, C.; Gallo, A. Reliable Use of Commercial Technology in High Temperature Environments. *Microelectron. Reliab.* **2000**, *40*, 1671−1678.
(59) Yu, Z.; Su, Y.; Gu, R.; Wu, W.; Li, Y.; Cheng, S. Micro-Nano Water Film Enabled High-Performance Interfacial Solar Evaporation. *Nano-Micro Lett.* **2023**, *15*, 214.
(60) Yu, Z.; Gu, R.; Tian, Y.; Xie, P.; Jin, B.; Cheng, S. Enhanced Interfacial Solar Evaporation Through Formation of Micro-meniscuses and Microdroplets to Reduce Evaporation Enthalpy. *Adv. Funct. Mater.* **2022**, *32*, 2108586.
(61) Lu, Q.; Zhao, X.; Jiang, Y.; Zhao, K.; Pan, J. Nano-Structured Urchin-Like Photothermal Covalent Organic Frameworks for Efficient Solar-Driven Interfacial Water Evaporation. *Chem. Eng. J.* **2024**, *499*, 156308.
(62) Yu, Z.; Gu, R.; Zhang, Y.; Guo, S.; Cheng, S.; Tan, S. C. High-Flux Flowing Interfacial Water Evaporation Under Multiple Heating Sources Enabled by a Biohybrid Hydrogel. *Nano Energy* **2022**, *98*, 107287.
(63) Wang, H.; Zhang, C.; Ji, X.; Yang, J.; Zhang, Z.; Ma, Y.; Zhang, Z.; Zhou, B.; Shen, J.; Du, A. Over 11 kg m-2 h-1 Evaporation Rate Achieved by Cooling Metal-Organic Framework Foam with Pine Needle-Like Hierarchical Structures to Subambient Temperature. *ACS Appl. Mater. Interfaces* **2022**, *14*, 10257−10266.
(64) Jiang, G.; Wang, L.; Tian, Z.; Chen, C.; Hu, X.; Peng, R.; Li, D.; Zhang, H.; Fan, P.; Zhong, M. Boosting Water Evaporation via Continuous Formation of a 3D Thin Film Through Triple-Level Super-Wicking Routes. *Mater. Horiz.* **2023**, *10*, 3523−3535.
(65) Lou, L.; Kang, Z.; Zhang, H.; Wang, P.; Fan, J. Nano-Capillary Aluminum Finned Heat Sink for Ultra-Efficient Evaporative Cooling. *Mater. Today Phys.* **2023**, *36*, 101175.
(66) An, N.; Zhang, X.; Chen, Y.; Wang, Z.; Qiu, J.; Gao, B.; Li, Q. A Self-Floating Photothermal/Photocatalytic Evaporator for Simultaneous High-Efficiency Evaporation and Purification of Volatile Organic Wastewater. *Adv. Funct. Mater.* **2025**, *35*, 2500777.
(67) Zhu, Z.; Wang, X.; Xing, S.; Tian, E.; Yin, T.; Liu, Y.; Kong, F. Fabrication of Highly-Stable Janus Hydrogel Evaporator with Customized Heat-Mass-Balance via Pore Engineering and Hofmeister Effect. *Chem. Eng. J.* **2025**, *514*, 163229.
(68) Guo, Y.; Zhao, X.; Zhao, F.; Jiao, Z.; Zhou, X.; Yu, G. Tailoring Surface Wetting States for Ultrafast Solar-Driven Water Evaporation. *Energy Environ. Sci.* **2020**, *13*, 2087−2095.
(69) Zhao, Z.; Li, J.; Wang, F.; Tan, P.; Wang, L.; Wang, B.; Jin, J.; Wang, X.; Zhang, W.; Wang, C. Drainage-Induced Arch Hydrogel-Based Interfacial Evaporator Drives Long-Term Stable Solar Evaporation. *J. Energy Chem.* **2025**, *104*, 540−550.

https://doi.org/10.1021/acsnano.6c06165
ACS Nano 2026, 20, 21281−21293

(70) Wang, R.; Su, Y.; Xiao, Z.; Wang, T.; Liu, K.; Gong, Z.; Wu, J.; Chen, J.; Liu, Z.; Li, J.; Zhang, Y. H.; Wang, L.; Li, B.; Zhang, X.; Li, C. Ternary Inclusion Co-Crystals for Efficient Photothermal Conversion and Solar-Driven Water Evaporation. *Adv. Sci.* **2025**, *12*, No. e2500050.
(71) Dong, W.; Tao, H.; Jiang, H.; Li, H.; Zhou, S.; Jia, S. Development of a Phase-Change Energy Storage Gel via Grafting for Efficient and Sustainable Solar-Driven Water Evaporation. *Chem. Eng. J.* **2025**, *512*, 162648.
(72) Jin, J.; Wang, C.; Wei, D.; Wang, B.; Lin, X.; Zhang, W.; Shi, C.; Zhao, Z.; Wang, L.; Wang, F. An Extremely Salt-Resistant Hydrogel-Based Solar Evaporator for Stable Saturated Brine Desalination. *Small* **2025**, *21*, No. e2411624.
(73) Lu, T.; Li, X.; Lv, W.; Bai, H.; Lu, M.; Qian, Z.; Lv, S. Durable and Highly Absorptive Ant-Nest Structured Superhydrophobic Sponge for Efficient De-Icing and Interfacial Evaporation in Polar Environments. *Mater. Horiz.* **2025**, *12*, 2899−2910.
(74) Yang, Y.; Wang, D.; Liao, W.; Zeng, H.; Wu, Y.; Li, L.; Feng, W.; Xue, J.; Cao, H.; Chen, J.; Huang, Y.; Zheng, Y.; Wang, P.; Liu, J.; Guo, M.; Zhou, H.; Fan, X. Arch-Bridge Photothermal Fabric with Efficient Warp-Direction Water Paths for Continuous Solar Desalination. *Adv. Fiber Mater.* **2024**, *6*, 1026−1036.
(75) Liu, Z.; Zhou, Z.; Wu, N.; Zhang, R.; Zhu, B.; Jin, H.; Zhang, Y.; Zhu, M.; Chen, Z. Hierarchical Photothermal Fabrics with Low Evaporation Enthalpy as Heliotropic Evaporators for Efficient, Continuous, Salt-Free Desalination. *ACS Nano* **2021**, *15*, 13007−13018.

https://doi.org/10.1021/acsnano.6c06165
ACS Nano 2026, 20, 21281−21293